Modeling of inter- and intra-ELM tungsten erosion during DIII-D H-mode discharges

G.L. Xu[1,2], J. Guterl[3], T. Abrams[4], H.Q. Wang[4], J.D. Elder[5], E.A. Unterberg[6], D.M. Thomas[4], P.C. Stangeby[4,5], H.Y. Guo[4*], M.Y. Ye[1*]

[1]*School of Physical Science, University of Science and Technology of China, Hefei, China*
[2]*College of Physics and Optoelectronic Engineering, Shenzhen University, Shenzhen 518060, China*
[3]*Oak Ridge Associated Universities, Oak Ridge, Tennessee, USA*
[4]*General Atomics, PO Box 85608, San Diego, CA 92186-5608, USA*
[5]*University of Toronto Institute for Aerospace Studies, Toronto, M3H 5T6, Canada*
[6]*Oak Ridge National Laboratory, Oak Ridge, TN 37830, USA*
* Corresponding authors, E-mail: guohy@fusion.gat.com, E-mail: yemy@ustc.edu.cn

Abstract:
The relationship between the tungsten gross erosion and the ELM characteristics is investigated for high performance (H-mode) discharges during the dedicated Metal Rings Campaign in DIII-D, using the one-dimensional 'free-streaming' ELM model, coupled to a simple analytical TRIM.SP sputtering model, while the OEDGE code is employed to calculate the inter-ELM impurity distribution and tungsten gross erosion. A carbon-tungsten mixed target material is used for both inter- and intra-ELM simulations. The OEDGE results reveal that the inter-ELM tungsten gross erosion rate is not sensitive to the carbon fraction on the tungsten surface layer; a wider range of carbon fractions from 0.3 to 0.6 give similar tungsten gross erosion profiles and match the diagnostic data, which is consistent with the simple analytical model. However, the intra-ELM simulation indicates that the value of surface carbon fraction can be as low as 0.3 to reproduce the measured tungsten gross erosion during ELMs, based on the effective ionizations/photon (S/XB) value of WI emissions. For both inter- and intra-ELM cases, carbon is predicted to dominate the tungsten erosion. However, in contrast to the inter-ELM tungsten erosion, which is dominated by locally redeposited C^{2+}, the energetic C^{6+} originating from the pedestal can contribute substantial tungsten erosion in the near-separatrix region during ELMs, and the width of this C^{6+} dominated region exhibits a negative correlation with the heat flux density carried by ELMs.

Key words: plasma material interaction, tungsten erosion, ELM

1. Introduction

Tungsten is chosen to be the divertor material for ITER [1] due to its low sputtering yields and low tritium retention. However, the strong radiation of high-Z impurities in the core plasma imposes a stringent limit to the tungsten core concentration, i.e., $\lesssim 10^{-5}$ [2]. It is essential to understand erosion mechanisms for the control of impurity sourcing.

ASDEX-Upgrade started armoring tungsten first wall components since 1999 and achieved a full tungsten first wall coverage in the year of 2007 [3]. JET transformed to an ITER-like first wall with a combination of beryllium main chamber

and tungsten divertor in 2011 [4]. Studies on both ASDEX-Upgrade and JET suggest an inhomogeneous tungsten poloidal erosion and deposition distribution, and the outer divertor as the most important tungsten source during the discharges [4–6]. Although ELMs are helpful to flush the tungsten impurity out of the confined plasma, they can also significantly increase the tungsten gross erosion on the divertor targets [7][8]. Thus, a careful study of both inter- and intra-ELM tungsten erosion mechanisms for H-mode discharges is needed.

Extensive research on plasma material interactions has been performed on DIII-D by leveraging the unique Divertor Materials Evaluation System (DiMES) [9]. Good agreement on tungsten gross erosion rate and distribution are achieved between modeling and experimental data for both L-mode and inter-ELM H-mode phases [10–12]. To understand tungsten erosion, redeposition and transport on a larger scale, a dedicated Metal Rings Campaign (MRC) [13] was carried out in DIII-D in 2016. In this campaign, two toroidally symmetric rings of tungsten-coated TZM tiles were inserted in the lower outer divertor, while all of the other PFCs remained un-coated graphite. Initial results on the W erosion during ELMs are reported in [14,15]. Ref. [14] focuses on using the target diagnostic data and a newly developed mixed material model to reproduce the intra-ELM averaged W erosion profiles across the tungsten ring, while Ref. [15] reports on validating the free streaming model (FSM) [16] predictions of W sputtering during ELMs near the strike point taking the target particle recycling process into consideration.

This paper is an extension of Ref. [14] to cover the type-I ELMy H-mode discharges with different ELM characteristics obtained from the MRC. The filtered camera data show that as ELM frequency increases, the tungsten erosion during ELMs becomes more important. To understand the inter-ELM tungsten erosion, the OEDGE (OSM-EIRENE-DIVIMP) code package [17] is employed with a new mixed material model incorporated into DIVIMP [18]. Moreover, a semi-analytic model based on the TRIM.SP [19] sputtering code is developed to study intra-ELM impurity sourcing on the tungsten ring.

The rest of the paper is organized as follows. The experimental setup is described in section 2. The analysis of the ELM characteristics with the FSM is presented in section 3. Inter- and intra-ELM tungsten erosion processes are discussed in section 4 and section 5, respectively, followed by a summary and discussion in section 6.

2. Experimental setup

As shown in figure 1, two sets of toroidally symmetric tungsten-coated metal insets were installed at the DIII-D outer lower divertor during the MRC, named as ‘floor ring’ (located at 1.320 m < r < 1.370 m) and ‘shelf ring’ (located at 1.405 m < r < 1.455 m), respectively. The shelf ring was relatively better diagnosed than the floor ring. Two new Langmuir probes [20] were installed on the shelf ring to measure local electron temperature and ion saturation current profiles. In addition, the shelf ring was imaged by a CCD camera with an exposure time of 10 ms, 100 Hz framing rate and ~0.8 mm spatial resolution. The WI 400.9 nm emission line is filtered to get information on the tungsten gross erosion via the S/XB method [12]. The lower outer divertor is covered by an infrared (IR) camera [21], which provides heat flux measurements with a high time resolution (0.1 ms). The Thomson scattering [22] and charge exchange recombination spectroscopy (CER) [23] provide the density of electron and C^{6+} at the outer midplane (OMP), respectively.

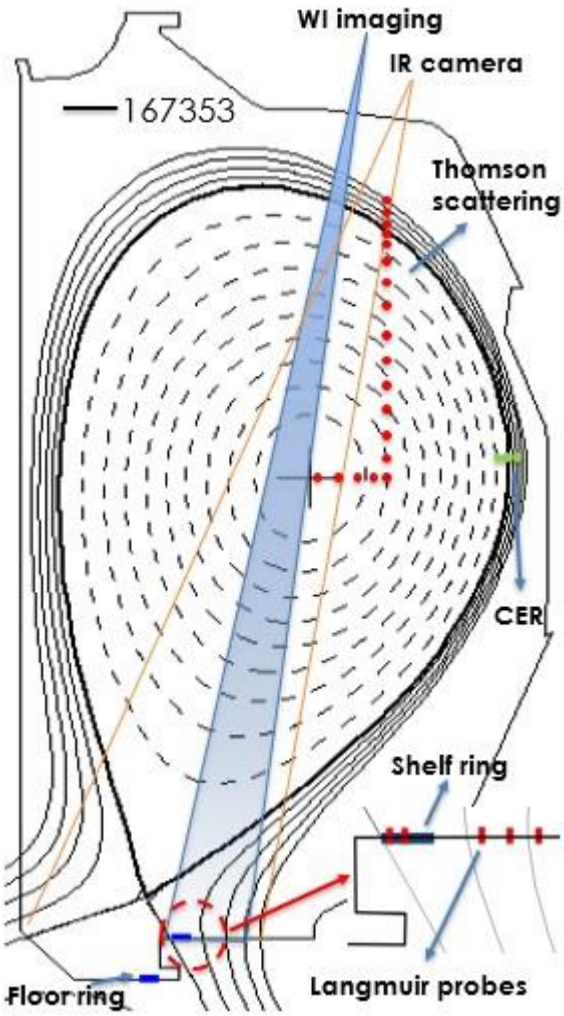

Fig. 1. The magnetic equilibrium of discharge 167353 at 3000 ms, the cross section of the main chamber, and the key diagnostics used in the metal rings campaign. The insert shows a magnified version of the shelf ring and Langmuir probes.

Three H-mode discharges with outer strike point fixed on the edge of the shelf ring are selected to study the tungsten erosion mechanisms. These three H-mode discharges have different ELM sizes and frequencies. Detailed information is listed in Table 1. Discharge 167353 and discharge 167358 have a similar pedestal electron density and temperature, while discharge 167321 has better energy confinement with a higher pedestal temperature. Based on the ELM frequencies and sizes, these three discharges are labeled as 'low frequency/large size' (167353), 'mid frequency/mid size' (167358) and 'high frequency/small size' (167321). The ELM frequencies of the chosen discharges are below the filtered camera framing rate, i.e., less than 100 Hz, to distinguish the intra-ELM from the inter-ELM filtered camera data.

Table 1. Pedestal and ELM parameters of H-mode plasmas selected for W erosion study

shot number	n_{ped} ($10^{19}m^{-3}$)	T_{e_ped} (eV)	f_{ELM} (Hz)	δW (MJ)	δW/W
167353	5.98	310	18	0.07	10%
167358	5.95	300	30	0.04	6%
167321	3.74	498	70	0.03	3%

3. Free-Streaming Model fitting

The Free-Streaming Model (FSM) is a simple analytic model developed by Fundamenski et al. to describe the ELM transport in the scrape-off-layer (SOL). In this simple model, the coulomb force is neglected in the parallel Vlasov equations. Assuming an initial Maxwellian distribution, this one-dimensional model can reproduce some of the main features of an ELM evolution. Recently, an extensive experimental validation of simple analytical predictions of the FSM has been done on JET H-mode discharges in a wide range of conditions [24]. By using the FSM, we can obtain more precise plasma conditions at the divertor target during ELMs to guide the intra-ELM simulation of tungsten sourcing.

In the FSM, the parallel particle and energy flux densities during an ELM are predicted as [25]:

$$\Gamma_{//} = \sqrt{2} n_0 c_s \frac{L/\delta_0}{(t/\tau_0)^2} e^{-\frac{(L/\delta_0)^2}{(t/\tau_0)^2}} \quad (1)$$

$$Q_{//} = \Gamma T_{\mathrm{i}} \left(\frac{(L/\delta_0)^2}{(t/\tau_0)^2} + 1 \right) \quad (2)$$

where n_0 and c_s are the electron density and deuterium ion sound speed at the pedestal top, L is the connection length between the midplane to the target, δ_0 is the initial parallel extension of ELM filaments, τ_0 is the ELM characteristic expansion time, t is the ELM evolution time in seconds, and T_i is the ion temperature at the target plane. We should note that in [25,26], the T_i is assumed to be the same value of the ion temperature at the pedestal top, but in this paper, the particle and energy flux densities from the experimental data are used to infer this parameter.

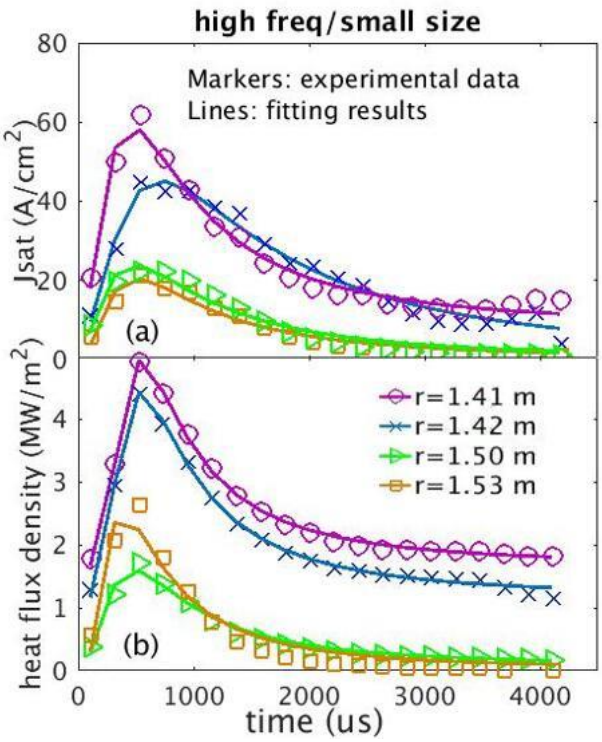

Fig. 2. The particle flux and heat flux density fitting results for different radial locations. (a) Markers are from Langmuir probe data and lines are fitting results using function (3). (b) Markers are from IR camera data and lines are fitting results using function (4).

Using N_0, τ_s, E_0 to represent $\sqrt{2} n_0 \tau_0 c_s$, L/c_s and $\sqrt{2} n_0 \tau_0 c_s T_i$ respectively, equation (1) and (2) can be rewritten as:

$$\Gamma_{//} = N_0 \frac{\tau_s}{t^2} e^{-\frac{\tau_s{}^2}{t^2}} + \Gamma_{inter_elm} \quad (3)$$

$$Q_{//} = E_0 \frac{\tau_s}{t^2} \left(\frac{\tau_s{}^2}{t^2} + 1 \right) e^{-\frac{\tau_s{}^2}{t^2}} + Q_{inter_elm} \quad (4)$$

including the background particle and energy flux densities, Γ_{inter_elm}, Q_{inter_elm}.

In this paper, the 1-D FSM is used to fit the ion saturation current (from Langmuir probe data) and heat flux density (from IR camera data) for different flux tubes in the SOL, where N_0, τ_s, E_0, Γ_{inter_elm}, and Q_{inter_elm} are free fitting parameters. The fitting results for discharge 167321 are shown in figure 2 as an example. By fitting the experimental data, the value of N_0, τ_s, E_0, Γ_{inter_elm} and Q_{inter_elm} for different radial locations can be obtained. We should note that, unlike the IR camera, the Langmuir probes are located at distinct radial locations, and thus the values inferred from the Langmuir probe data are linearly interpolated to infer values for other radial locations.

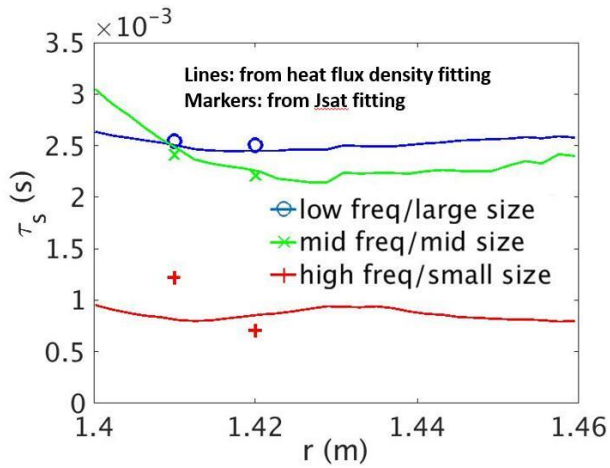

Fig. 3. The ELM transport time from the OMP to the target for different radial flux tubes. The lines are from the heat flux density fitting results, and the markers are from the particle flux density fitting results.

Note that both formula (3) and formula (4)

contain τ_s (the ELM transport time from the OMP to the target). Figure 3 compares the best-fit τ_s values based on the particle flux and heat flux to the metal ring region for all three discharges. Good agreement (within 30%) is achieved between these two fitting methods. Moreover, the ELM transport time from the OMP to the target is shown to be less than 3 ms, and is smaller for the discharge (167321) with 'high frequency/ small size' ELMs due to the higher pedestal temperature (higher deuterium ion sound speed).

The ELM transport time from OMP to the target is mainly determined by the magnetic perturbation near the X point, which makes the connection length 5-10 times larger than the unperturbed one [27–29]. During an ELM burst, the energetic ions, including high charge state C^{6+}, which are ejected from the pedestal region, transport along the magnetic field line to the target. Both deuterium and carbon can be trapped near the X point region, despite that the sound speed of carbon is slower. The magnetic perturbation disappears when deuterium ions arrive at the divertor target. Then, carbon ions can quickly reach the target from the X point region by following unperturbed magnetic field lines. Hence, the time difference between the arrival of deuterium and carbon ions to the target can be neglected comparing with the total ELM transport time. Therefore, we assume that fully stripped carbon ions are transported within the deuterium ELM filaments.

As discussed in [14], an ELM transport time of 3 ms is not sufficiently long for energetic C^{6+} to recombine into lower charge states under typical DIII-D edge plasma conditions. Therefore, most of the energetic carbon ions remain fully stripped when arriving at the divertor target during ELMs for all these three chosen discharges.

Table 2. Parameters and descriptions in the FSM

Symbols	Meaning	Value
n_0	Electron density at the pedestal top	Directly measured by Thomson Scattering
c_s	Deuterium ions' sound speed at the pedestal top	$\sqrt{(T_e+T_i)/m_D}$, *Te* and *Ti* are from Thomson scattering and CER respectively
L	Connection length between the OMP to the target	$\tau_s c_s$
δ_0	Initial parallel extension of ELM filaments	$N_0/(\sqrt{2}n_0 c_s)$
τ_0	ELM characteristic expansion time	δ_0/c_s
T_i	Ion temperature at the divertor target	E_0/N_0

All the other parameters in the FSM can be inferred after obtaining the value of N_0, τ_s, and E_0, as listed in Table 2. The profiles of ELM-averaged *Ti* (E_0/N_0) across the tungsten ring are shown in figure 4. Then, the electron density at the target can be estimated by

$$n_{intra-ELM} = \frac{J_{sat}}{\sqrt{\frac{T_i+T_e}{m_i}}} \quad (5)$$

where the ELM-averaged J_{sat} and T_e are obtained from Langmuir probes, which are found to be capable of measuring the electron temperature during ELMs [24,30,31].

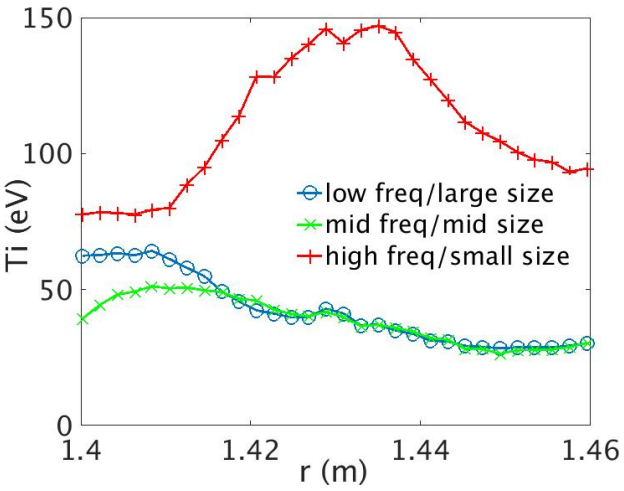

Fig. 4. The ion temperature profiles on the shelf ring, obtained from the FSM fitting.

The target density can also be obtained from the FSM [26]:

$$n(t) = n_0 \frac{\delta_0}{\delta(t)} e^{\frac{-L^2}{2\delta(t)^2}} \quad (6)$$

where $\delta(t) = \delta_0\sqrt{1 + (t/\tau_0)^2}$.

The ELM averaged electron density is given by:

$$n_{FSM} = \frac{\int_{ELM} n(t)dt}{\Delta t_{ELM}} + n_{inter-ELM} \quad (7)$$

including the electron density between ELMs, $n_{inter\text{-}ELM}$, since the FSM does not take into account the influence of the background plasma. Hence, the ELM-averaged electron density profiles can be determined by applying equation (7) to different flux tubes.

Figure 5 shows a comparison of the ELM-averaged electron density profiles on the shelf ring obtained from the two methods described above. For all three discharges, a relatively good agreement (within 20%) is achieved between these two methods, giving confidence to these measurements of the ELM-averaged electron densities.

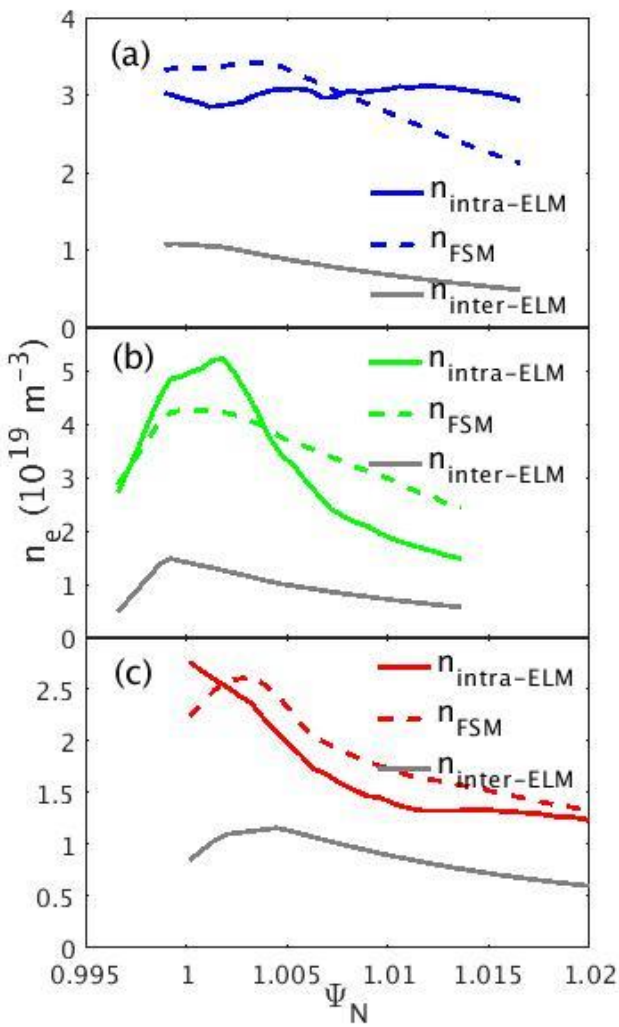

Fig. 5. The ELM-averaged electron density on the shelf ring obtained from equation (5) and equation (7), together with the electron density between ELMs, for the discharges with (a) the 'low frequency/large size', (b) the 'mid frequency/mid size', and (c) the 'high frequency/small size' ELMs.

The intra-ELM and inter-ELM tungsten WI 400.9 nm emission data are manually distinguished from the filtered camera raw data with the background signal subtracted. Previous DIII-D DiMES experimental data shows that the tungsten effective ionizations/photon (SX/B) value has a strong positive correlation with the electron density, especially when the electron density is high [12]. Therefore, it is very important to accurately measure the electron density before calculating the intra-ELM tungsten gross erosion rate. The tungsten

effective S/XB value was obtained from the ADAS database [32] by using the electron density inferred from equation (5) (T_i obtained from FSM analysis during ELMs and $T_i = T_e$ between ELMs), as well as the electron temperature from Langmuir probe data. Then W gross erosion (Γ_W) was calculated from WI emission data (I_{WI}) by

$$\Gamma_W = \frac{S}{XB} I_{WI} \quad (8)$$

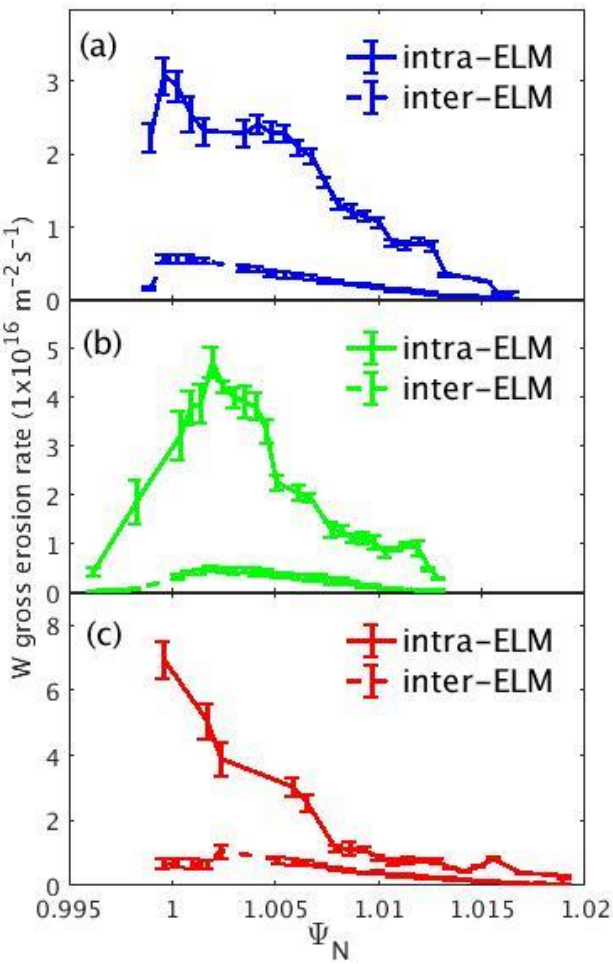

Fig. 6. The intra- and inter-ELM tungsten gross erosion profiles with error bars. (a) The 'low frequency/large size-ELM' discharge; (b) the 'mid frequency/mid size-ELM' discharge; (c) the 'high frequency/small size-ELM' discharge.

The intra- and inter-ELM averaged tungsten gross erosion profiles for the three discharges are shown in figure 6. The intra-ELM tungsten gross erosion rate is 5-10 times larger than that between ELMs. The contribution of intra-ELM tungsten gross erosion to the total tungsten erosion can be calculated by taking into account the ELM duration time. As shown in figure 7, the intra-ELM tungsten erosion makes a significant contribution to the total W erosion for all these three discharges, and the intra-ELM W erosion ratio seems to have a positive correlation with the ELM frequency, similar to the previous JET-ILW results [33]. This is because the increase of ELM frequency usually increases the total intra-ELM time, thus making intra-ELM erosion more important.

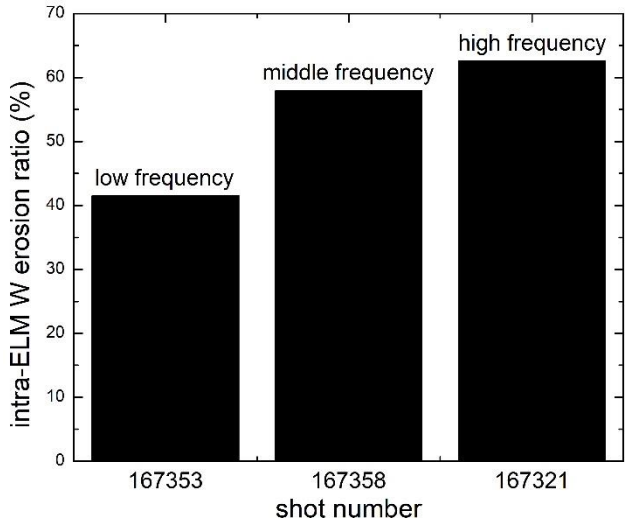

Fig. 7. The ratio of integrated intra-ELM tungsten gross erosion to the total tungsten gross erosion for the discharges with 'low frequency/large size', the 'mid frequency/mid size' and the 'high frequency/small size' ELMs.

4. Inter-ELM simulation

4.1. Analytic mixed material model

Although DIII-D had tungsten rings on the outer lower divertor region during the MRC, the rest of the first wall remained graphite, which made the carbon impurity the most important impurity present in the DIII-D plasma. Together with deuterium, the carbon impurity can impact the tungsten surface and cause tungsten erosion.

Moreover, carbon may deposit on the tungsten surface and thus create a carbon-tungsten mixed material.

Another important process that should be considered is the carbon reflection on the tungsten surface. Since carbon has a high reflection ratio (near 0.6 for 400 eV impact energy and 45° impact angle [34]) and a high redeposition fraction (ratio of eroded C flux to that redeposited onto the surface), ~ 0.7 according to the DIVIMP calculations for these cases). Note that the reflection process may significantly increase the total carbon flux to the target surface.

Due to the ion temperature gradient (ITG) force, the upstream carbon impurity may be readily trapped in an ITG-dominated region [35], therefore making the near-target redeposited carbon flux the most important part of the total carbon flux to the target. Considering the reflection effect and ignoring the carbon from cross field transport and carbon self-sputtering, which contribute to less than 10 percent of the total erosion from the DIVIMP calculation, the carbon flux to the target is approximated by:

$$\Gamma_C \approx \Gamma_{Credeposited} = \frac{\alpha f Y_{C_D} \Gamma_D}{1-\alpha R_{C_t}} \quad (9)$$

where α is the C redeposition fraction; f is the carbon fraction on tungsten surface; Y_{C_D} is the C sputtering yields from D impact; Γ_D is the deuterium particle flux to the target; and R_{Ct} is the averaged carbon reflection coefficient.

$$R_{Ct} = (1-f)R_{C_W} + fR_{C_C} \approx (1-f)R_{C_W} \quad (10)$$

where R_{C_W} and R_{C_C} are the C reflection coefficient on W and C respectively. R_{C_W}= 0.6 and R_{C_C} = 0.005 for 400 eV C impact energy and 45° impact angle.

The W gross erosion rate is given by:

$$\Gamma_W = (1-f)Y_{W_C}\Gamma_c = (1-f)Y_{W_C}\left(\frac{\alpha f Y_{C_D}\Gamma_D}{1-\alpha R_{C_t}}\right) = \frac{(1-f)\alpha f}{1-0.6\alpha+0.6\alpha f}\Gamma_D Y_{C_D} Y_{W_C} \quad (11)$$

where Y_{W_C} is the W sputtering yield from impinging carbon.

If we use β in place of $\frac{(1-f)\alpha f}{1-0.6\alpha+0.6\alpha f}$, which represents the carbon erosion, redeposition and refection processes, then the equation (11) can be rewritten as

$$\Gamma_W = \beta \Gamma_D Y_{C_D} Y_{W_C} \quad (12)$$

Considering a fixed background plasma, the value of $\Gamma_D Y_{C_D} Y_{W_C}$ is constant, so that the tungsten sputtering yield is proportional to β. From the DIVIMP calculation, the outer target carbon redeposition fractions for all these three discharges are in the range of 0.6-0.8. Figure 8 shows the β value for different carbon surface fractions (f) and different carbon redeposition fractions (α). As can be seen, the tungsten erosion rate shows a nonlinear relationship with the carbon fraction on the tungsten surface. On the one hand, a higher carbon surface fraction increases the carbon flux to the target, thus increasing the tungsten erosion. On the other hand, the increase of carbon surface fraction can act as a protection layer against tungsten sputtering. Therefore, the total tungsten erosion first increases with the carbon surface fraction increasing, then decreases when the carbon surface fraction is sufficiently large so that the carbon protection effect becomes dominant.

Previous studies of carbon impurity behavior on tungsten plasma facing surface revealed that C may accumulate at the tungsten surface layer with the surface density ratio ranging from 0.3 to

0.6 [36–38]. Figure 8 shows that the value of β does not change significantly with f varying in the range of 0.3-0.6. This suggests that the tungsten erosion rate is actually not sensitive to the carbon fraction on the tungsten surface.

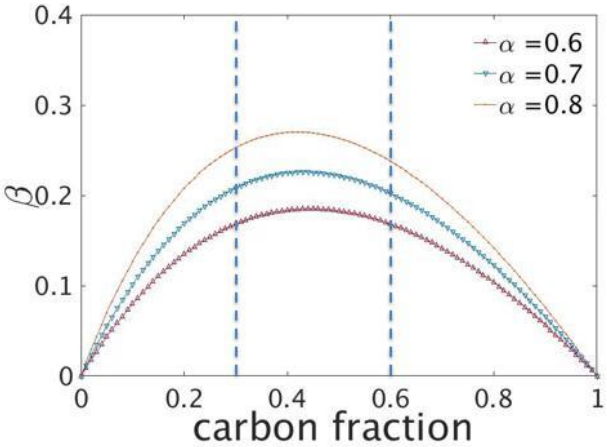

Fig. 8. The relationship between β and carbon fraction on the tungsten surface (f) for the different carbon redeposition fractions, 0.6, 0.7 and 0.8 respectively. β is not sensitive to the carbon fraction for $0.3<f<0.6$.

4.2. OEDGE simulation

The target plasma parameters (J_{sat} and T_e from Langmuir probes and fitted by the Eich function [39]) are set as input to the onion skin model (OSM) to generate the background plasma. The usage of target diagnostic data is favorable for generating a realistic near target background plasma benefiting the target material erosion simulation. After obtaining the background plasma, the radial profiles of carbon and tungsten erosion are sequentially calculated by using the Monte Carlo impurity tracking code DIVIMP [18].

To simulate the inter-ELM tungsten erosion process, a new mixed material model is incorporated into the DIVIMP code [14]. In this mixed material model, the carbon fraction on the tungsten surface can be set to a constant value between 0.0 and 1.0. The carbon reflection process is also included in the model. The carbon erosion is caused by both deuterium impact and carbon self-sputtering. The mixed material model is used in the tungsten ring region, with other plasma facing components remaining pure graphite. Since the angle between the magnetic field and the surface of the divertor target is about 1.5º at the outer strike point, non-normal incidence of plasma particles to the target surface may occur [40]. Therefore, the sputtering yields data of both carbon and tungsten are taken from [34] with the assumption of 45° impinging angle, same as the assumption made in [12].

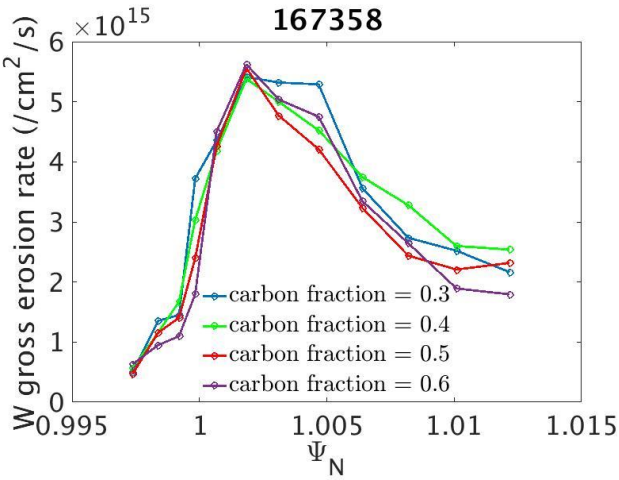

Fig. 9. The inter-ELM tungsten gross erosion profiles from OEDGE simulation results with carbon fraction on the tungsten surface set to be 0.3, 0.4, 0.5 and 0.6, respectively.

To examine the influence of carbon surface fraction on the total tungsten erosion and to validate result of the simple analytic model, the carbon surface fraction is adjusted from 0.3 to 0.6 in the DIVIMP code. Figure 9 shows the results of OEDGE simulation for the discharge 167358. The tungsten gross erosion rate from OEDGE results is not sensitive to the carbon fraction on the tungsten surface for f in the range of 0.3-0.6, which is consistent with the result of the simple analytic model in Section 4.1. Therefore, a carbon surface fraction of 30% is chosen to simulate the inter-ELM tungsten erosion process for all the three discharges.

Good agreements between experimental

measurement of tungsten gross erosion profiles and the OEDGE simulation results are achieved for all these three discharges, as shown in figure 10. The inter-ELM tungsten erosion is mainly caused by local eroded carbon flux, with about a 10% tungsten self-sputtering contribution, while the contribution from deuterium impinging is at a negligible level.

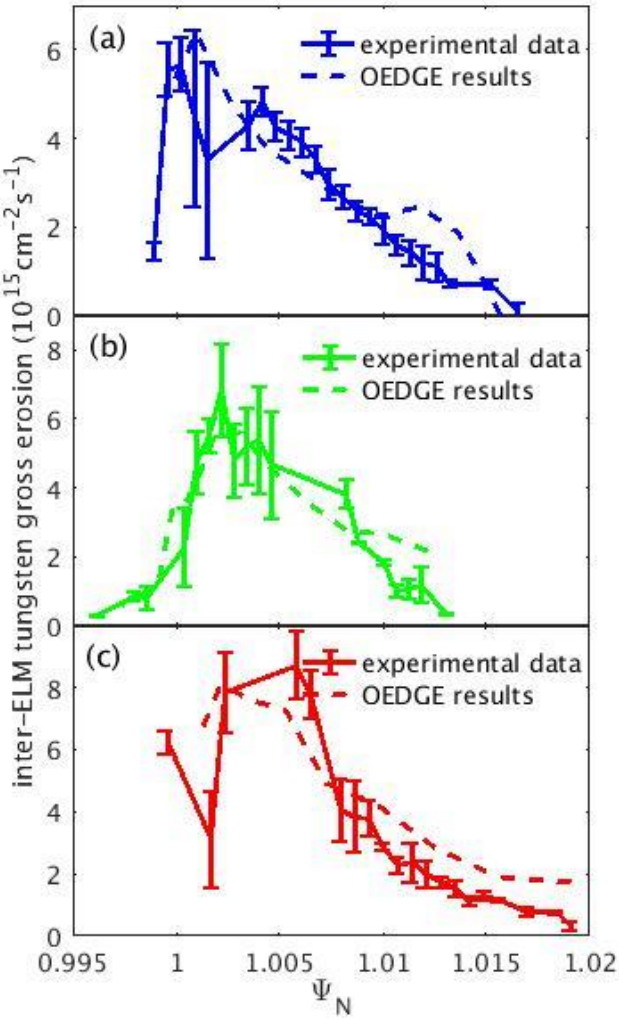

Fig. 10. The inter-ELM tungsten gross erosion profiles from experimental data and OEDGE simulation results with carbon fraction on the tungsten surface set to be 30%. (a) discharge 167353; (b) discharge 167358; (c) discharge 167321.

5. Intra-ELM simulation

5.1. Inferring Intra-ELM C^{6+} densities from CER data

The electron temperature at the pedestal top is above 300 eV for all three discharges studied, as shown in Table 1. Because of the high electron temperature inside of the pedestal region, the dominant charge state of the carbon impurity is C^{6+}. When an ELM occurs, the C impurity transports into the SOL region together with high energy D^+ particles.

The CER spectroscopy system [23] can be used to measure the C^{6+} density. The desired signal for this spectroscopic measurement is produced by charge exchange between neutrals in the neutral beams and ions in the plasma. Since the time resolution of the CER system (5 ms) is too large to distinguish ELM signals, we have developed a new method for inferring the intra-ELM C^{6+} density at the OMP.

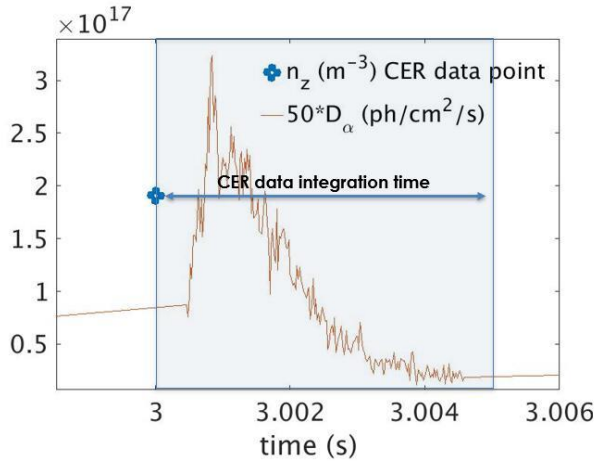

Fig. 11. The schematic plot of the possible time difference between the CER data point and the ELM burst time. The time resolution of CER system is 5 ms.

Here, the CER measurements before the ELM onset are chosen for analysis. Figure 11 shows the CER signal's integration time frame compared with the intra-ELM D_α signal from the divertor filterscope for the 'high frequency/small size' discharge (167321). Here we define *dt* as the time difference between the rise of CER signal and the start of ELM, as inferred from divertor filter scope D_α data:

$$d_t = t_{elm_start} - t_{CER} \quad (13)$$

We assume the OMP C^{6+} density increases instantly to a peak value after the ELM burst then exponentially decays to the inter-ELM C^{6+} level. For a specified Ψ_N, the C^{6+} density during an ELM can be expressed as:

$$n_{C6+}(t) = \frac{(\mathrm{sgn}(t)+1)}{2} n_{elm} e^{\frac{-t}{t_{telm}}} + n_{c0} \quad (14)$$

where n_{elm} is the C^{6+} peak density carried by an ELM; t_{elm} is the decay time and n_{c0} is the averaged C^{6+} density between ELMs.

The CER measurement can be expressed in terms of *dt* by:

$$n_{CER}(dt) = \left(\frac{(\mathrm{sgn}(t_{CER}-(dt-t_s))+1)}{2} t_{elm} n_{elm}\left(1 - e^{\frac{dt-t_s-t_{CER}}{t_{telm}}}\right) + n_0 t_{CER}\right)/t_{CER} \quad (15)$$

where $t_{CER} = 5$ ms, is the CER time resolution and t_s is the characteristic ion transport time from the OMP to the target, representing the time difference between the ELM start time observed at the OMP and the target.

If n_{elm}, t_{elm}, t_s and n_0 are treated as fitting parameters, the CER experimental data can be fitted by formula (15). Figure 12 shows the CER data points as well as the fitting result for the 'high frequency/small size' discharge at Ψ_N =1.004. From the fitting result, we can infer the ELM averaged C^{6+} density at the location of Ψ_N =1.004 on the OMP by using formula (16).

$$n^{C6+}_{intra-ELM} = \frac{\int_{ELM} n_{C6+}(t)dt}{\Delta t_{ELM}} = \frac{\int_{ELM} \frac{(\mathrm{sgn}(t)+1)}{2} n_{elm} e^{\frac{-t}{t_{telm}}} dt}{\Delta t_{ELM}} + n_{c0} \quad (16)$$

where n_{elm}, t_{elm} and n_0 are from fitting results.

Table 3. Parameters obtained from fitting results

shot number	Ψ_N	n_{elm} (m^{-3})	t_{elm} (s)	n_0 (m^{-3})	$n^{C6+}_{intra-ELM}$(m^{-3})	n_{e_ELM}(m^{-3})	c_{C6+}
167353	1.001	1.00E+18	0.0033	6.00E+16	5.08E+17	2.50E+19	2.03E-02
167358	1.002	4.16E+17	0.010	6.30E+16	3.95E+17	1.64E+19	2.41E-02
167321	1.004	5.40E+17	0.0013	6.39E+16	2.59E+17	1.10E+19	2.35E-02

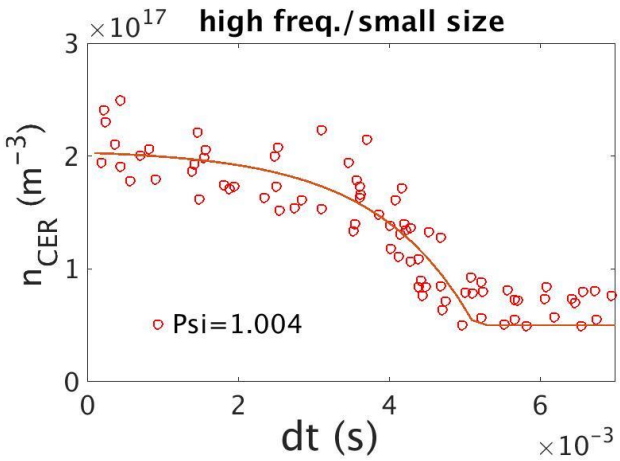

Fig. 12. The CER C^{6+} density data at Ψ_N =1.004 plotted against the time delay between the CER signal at OMP and the divertor D_α signal at the onset of an ELM (*dt*), and that fitted by function (15), for the 'high frequency/small size' discharge (167321).

The same method is applied to the other two discharges for the CER view chord closest to the separatrix and the results are listed in Table 3. The ELM averaged electron density (n_{e_ELM}) at the corresponding locations can be obtained from Thomson scattering data, so that the intra-ELM averaged C^{6+} concentration (c_{C6+}) at the OMP near the separatrix can be acquired. As listed in Table 3, the near separatrix C^{6+} concentration is about 2% in the ELM filaments for all three discharges.

5.2. Intra-ELM tungsten erosion from a semi-analytic model

A semi-analytic model based on TRIM.SP [19] has been developed to study tungsten gross erosion process during the ELMs [14]. In this model, the free-streaming ions, including D^+ and C^{6+}, are considered as the cause of the divertor target tungsten erosion. These energetic particles will also lead to large amount of carbon erosion on the carbon-tungsten mixed material. The redeposited carbon ions originating from the target carbon erosion can then further enhance the tungsten erosion. Since no intra-ELM background plasma is available for DIVIMP to simulate the carbon redeposition fraction, in this semi-analytic model, the carbon redeposition fraction is assumed to be 0.7 (the averaged value from inter-ELM DIVIMP simulations). The carbon erosion, redeposition and reflection processes are considered in the modeling, as described in Section 4.1. These promptly redeposited carbon ions are mainly in low charge states, thus C^{2+} is used to represent the locally redeposited carbon ions.

In the semi-analytic model, the free-streaming C^{6+} is assumed to exponentially decay in the radial direction, and the profile is described by two parameters. One is the C^{6+} concentration at the strike point, which is set to be the same value as the intra-ELM C^{6+} concentration at the OMP separatrix, as listed in Table 2: 2.03% for the 'low frequency/ large size' discharge; 2.41% for the 'mid frequency/mi size' discharge and 2.35% for the 'high frequency/small size' discharge. The other parameter η is used to adjust the radial decay length of free-streaming C^{6+} concentration. η is defined as the ratio of C^{6+} decay length divided by the decay length of D^+, where the intra-ELM decay length of D^+ can be obtained by fitting the Langmuir probe J_{sat} data to the Eich function [39]. By adjusting the value of η, different C^{6+} profiles can be achieved in the model.

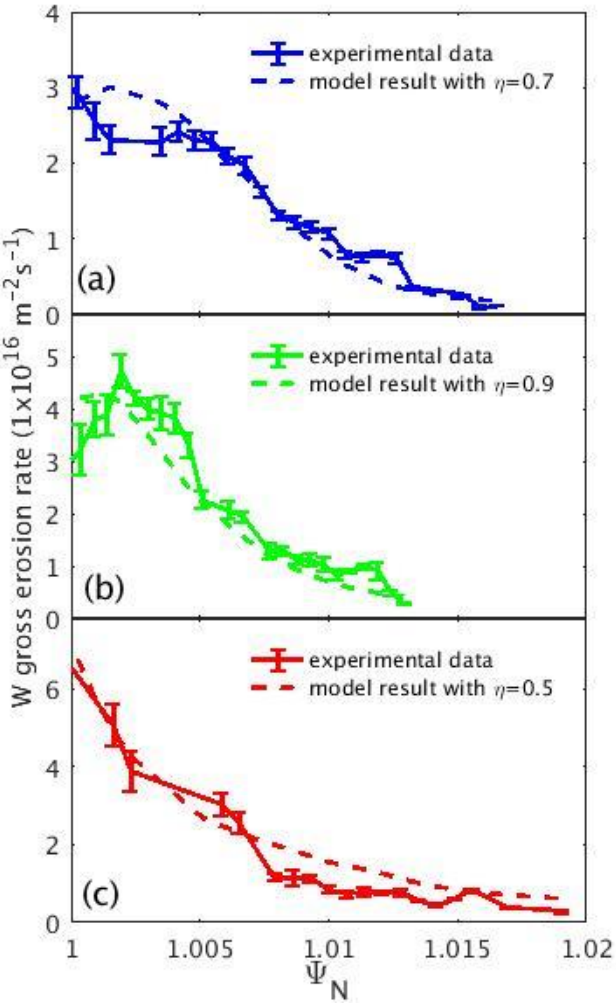

Fig. 13. The intra-ELM tungsten gross erosion profiles for $\Psi_N > 1.0$. The solid lines are the experimental data, and the dashed lines are the results from the semi-analytic model with η set to be 0.7, 0.9 and 0.5 for the (a) 'low frequency/large size' discharge, (b) 'middle frequency/mid size' discharge and (c) 'high frequency/small size' discharge, respectively.

Unlike the inter-ELM W erosion simulation, in which the OEDGE code is used to generate the background plasma and trace the impurity transport, in the intra-ELM semi-analytic model, we are trying to use the diagnostic data to reproduce the W erosion profiles. All input parameters in the semi-analytic model are either from the diagnostic data or from reasonable analysis as described above, except two adjustable parameters: f (carbon fraction on the carbon-tungsten mixed material surface) and η (

the ratio of C^{6+} decay length to D^{+} decay length). By adjusting the value of f and η, we hope to reproduce the intra-ELM tungsten erosion profiles and get some physics insights of the erosion mechanisms.

The intra-ELM tungsten gross erosion profiles from model results are shown in Figure 13, with the assumption of 30% carbon fraction on the tungsten surface. Good agreements are achieved between the model results and the experimental data for all these three discharges. The value of η, which represents the relatively radial decay length of C^{6+} compared with the D^{+}, varies from 0.5 to 0.9. Note that C^{6+} density exhibits the slowest decay rate for middle frequency, middle sized ELMs, which is related to the peak heat flux density during ELMs, as discussed in the next section.

5.3. Analysis of the intra-ELM tungsten erosion mechanism

In the previous nonlinear BOUT++ simulation of particle and heat fluxes during ELMs [41–43], the radial particle flux density for specified ion ι can be defined as:

$$\Gamma_{\iota r} = \langle n_\iota V_r \rangle = \langle n_\iota \frac{(b_0 \times \nabla \Phi)_r}{B_0} \rangle + \langle n_\iota \delta V_{\iota //} (\frac{b_0 \times \nabla A_{//}}{B_0}) \rangle \quad (17)$$

here <> means flux surface average; n_ι is the density of ι ions; V_r is the radial anomalous velocity; b_0 is the unit vector of magnetic field; Φ is the electric potential; B_0 is the magnetic field on axis; $\delta V_{\iota //}$ is the perturbed parallel velocity of ι ions and is proportional to the parallel velocity of ι ions; $A_{//}$ is the perturbed parallel vector potential. The first term is derived from the radial component of ExB drift and the second term represents the radial component of the perturbed magnetic field in the parallel particle flux contribution.

The ion radial decay length is proportional to the radial anomalous velocity:

$$\lambda_\iota \sim V_r \frac{L}{c_s} \sim \frac{\Gamma_{\iota r}}{n_\iota} \sim \langle \frac{(b_0 \times \nabla \Phi)_r}{B_0} \rangle + \langle \delta V_{\iota //} (\frac{b_0 \times \nabla A_{//}}{B_0}) \rangle \quad (18)$$

$\frac{L}{c_s}$ is the ELM transport time from the out OMP to the target. As discussed in section 5.2, the transport time is mainly determined by the magnetic perturbation near the X point, thus for different ions, their transport time are the same. For D^{+} and C^{6+}, the only difference is the $\delta V_{\iota //}$ in the perturbed magnetic field term. Considering the different value of $\delta V_{\iota //}$ as well as the possible weights of the two terms, the value of $\eta = \frac{\lambda_{C6+}}{\lambda_{D+}}$ should be in the region of $(\frac{1}{2\sqrt{2}}, 1)$. The more the value of the perturbed magnetic field part is weighted, the smaller the value of η becomes. The magnetic perturbation term is proved to be closely connected with the parallel energy flux density. A larger parallel energy flux density will help to achieve a larger radial transport due to magnetic flutter and the flux density due to ExB drift is not affected [41]. Therefore, the larger the intra-ELM parallel energy flux density, the more the perturbed magnetic field part in equation (18) will weight, thus a smaller η is expected.

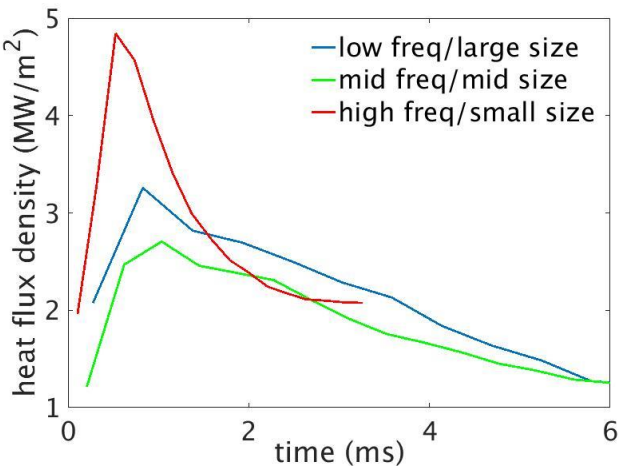

Fig. 14. The time evolution of the perpendicular heat flux density on the strike point for the low frequency/large size discharge (blue line), mid frequency/mid size discharge

(green line) and high frequency/small size discharge (red line).

The discharge-averaged intra-ELM heat flux density for all these three discharges can be derived from the IR camera data, and the time evolution of heat flux density on the strike point is shown in Figure 14. As shown in Figure 13, with the high pedestal top electron temperature, the 'high frequency/small size' discharge (167321) has the biggest peak heat flux density during ELMs, i.e., > 4 MW/m^2, while the 'mid frequency/mid size' discharge (167358) has the smallest peak heat flux density < 3 MW/m^2. Thus, the value of η for these three discharges should satisfy $\eta_{167321} < \eta_{167353} < \eta_{167358}$, which is consistent with the semi-analytic model fitting results showing in Figure 13.

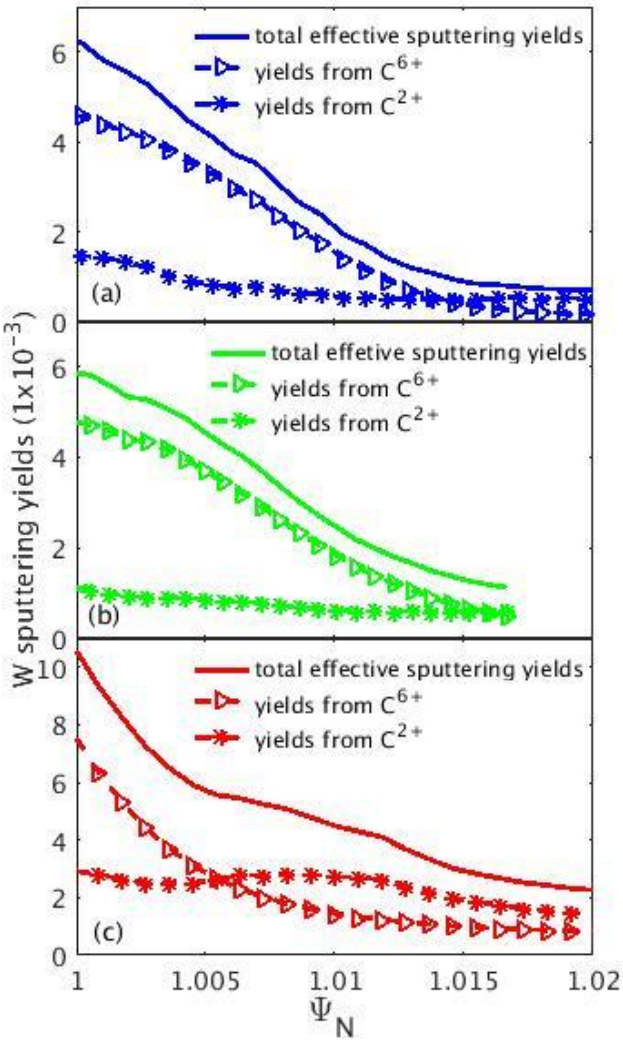

Fig. 15. The intra-ELM W gross erosion rates and contributions from energetic C^{6+} ions and locally redeposited C^{2+} ions for (a) the 'low frequency/large size' discharge, (b) the 'mid frequency/mid size' discharge and (c) the 'high frequency/small size' discharge.

Figure 15 plots the total W effective sputtering yields together with the contributions from energetic streaming C^{6+} and local recycling C^{2+}. Due to the low impact energy of D^+, the W sputtering yield from D^+ is much smaller than that from carbon and is not shown in this figure. The energetic C^{6+} dominates the W erosion at the strike point. However, since the C^{6+} flux radially decays, the contribution from C^{6+} dramatically decreases across the tungsten ring. Therefore, the tungsten erosion can be divided into two regions: one is the near separatrix region in which the tungsten erosion is dominated by the energetic C^{6+} streaming from the pedestal; the other is the outer SOL region, where the local recycling C^{2+} dominates the tungsten erosion.

The profiles of the effective sputtering yields contributed by local C^{2+}, which is strongly related to the local electron temperature, is relatively flat. As discussed in [14], the radial tungsten erosion profile is determined largely by the C^{6+} concentration much more than the change of impact energy. As a result, the width of the C^{6+} dominated region is dependent on two parameters: the C^{6+} concentration at the strike point and the relative decay length η. Compared to other two discharges, the 'mid frequency/small size' discharge has the largest η and strike point C^{6+} concentration, thus leading to the widest C^{6+} dominated region. The 'high frequency/small size' discharge has the smallest η, and thus the narrowest C^{6+} dominated region.

Carbon surfaces have a much lower threshold sputtering energy relative to tungsten for both deuterium and carbon impacts. The recycling C^{2+} can be created by free-streaming C^{6+} as well as

D^+ impinging on the carbon-tungsten mixed material. Since the C^{6+} flux is much lower than the D^+ and the concentration radially decays, the carbon erosion is dominated by the free-streaming D^+ especially in the outer SOL region. From the model results, the carbon erosion caused by impinging D^+ is more than 5 times larger than that caused by C^{6+} at Ψ_N>1.01 for all these three discharges. Therefore, during ELMs, the energetic C^{6+} dominates the tungsten erosion near the separatrix, while the free-streaming D^+ dominates the tungsten erosion in the outer SOL region.

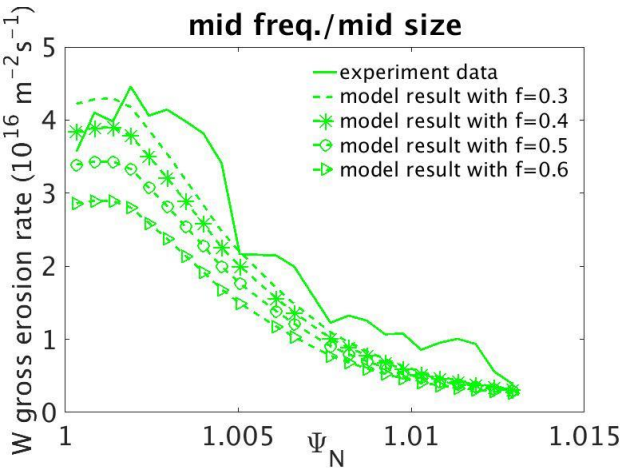

Fig. 16. The intra-ELM tungsten gross erosion profiles for Ψ_N > 1.0. The solid lines are the experimental data, and the dashed lines are the results from the semi-analytic model with the carbon fraction on the tungsten surface set to be 0.3, 0.4, 0.5 and 0.6 for the 'mid frequency/mid size' discharge.

It is worth noting that in Section 4.1 and Section 4.2, we found that the inter-ELM W gross erosion simulation results are robust to a wide range of carbon surface fractions ($0.3 \leq f \leq 0.6$) and the tungsten erosion is mainly caused by the locally eroded carbon flux. However, in contrast to the inter-ELM phase, the change of carbon surface fraction exhibits an obvious influence on the total tungsten erosion during ELMs, especially in the near separatrix region, as shown in Fig. 16 for the discharge with 'mid frequency/mid size' ELMs. In that region, the tungsten erosion is mainly dominated by the streaming energetic C^{6+}. Increasing the fraction of carbon means decreasing the tungsten fraction on the mixed material, thus decreasing the tungsten erosion caused directly by the impinging C^{6+}. Therefore, in the intra-ELM simulation, the tungsten erosion is sensitive to the carbon fraction on the tungsten surface. The modeling of the experimental data with the semi-analytic model, as shown in Fig. 13, further indicates a carbon fraction of 30% on the tungsten surface, which is on the lower bound found in inter-ELM simulations.

6. Summary and Discussion

H-mode tungsten erosion processes have been investigated for the discharges with varying type I ELM sizes ($\Delta W/W$ ranging from 3% to 10%) and ELM frequencies (18 Hz to 70 Hz) conducted during the DIII-D Metal Rings Campaign. The one-dimensional FSM model is used to analyze the ELM transport time and electron density at the target plate. The ELM transport time is used to evaluate the charge state of C originating from the H-mode pedestal, and the divertor electron density is used to accurately calculate the effective ionizations/photon (S/XB) value of the tungsten influx during ELMs. Then a semi-analytical model based on the TRIM.SP sputtering code is used to simulate the intra-ELM tungsten gross erosion profiles. The OEDGE code is employed to calculate the inter-ELM impurity distribution and tungsten gross erosion.

The WI imaging experimental data showed that the intra-ELM W erosion rate can be 5-10 times larger than the inter-ELM phase. Thus, the intra-ELM W erosion can be comparable to the inter-ELM phase and even dominate the total tungsten erosion, despite the short ELM duration. The ratio of W erosion during ELMs to the total W erosion can be more than 60%, and increases

with the ELM frequency, since increasing the ELM frequency usually increases the ratio of ELM time to the total discharge time.

Due to the presence of carbon in DIII-D, a carbon-tungsten mixed material models are used for both inter- and intra-ELM tungsten gross erosion simulations. For the inter-ELM phase, the modeling results suggest that tungsten is mainly eroded by the local recycling carbon flux, which mostly originates from the erosion of the carbon-tungsten mixed material. The increase of the carbon surface fraction increases tungsten erosion, which can be, however, offset by the coverage of carbon on the tungsten rings. Both the OEDGE code and the simple analytic model show that the inter-ELM W gross erosion is not sensitive to the carbon surface fraction in the range of $0.3<f<0.6$.

In contrast to the inter-ELM tungsten erosion, the intra-ELM tungsten erosion is sensitive to the carbon surface fraction, especially in the near separatrix region. A carbon surface fraction of 0.3 can yield a good agreement between simulations and experimental measurements of intra-ELM W gross erosion profiles for all the different H-mode discharges modeled. This further indicates that the carbon surface fraction on the tungsten ring can be as low as 30%.

The simulations indicate that the streaming energetic C^{6+} originating from the pedestal region remain fully stripped when arriving at the divertor target during ELMs, causing large amounts of tungsten erosion, and dominating the tungsten erosion in the near separatrix region. However, in the outer SOL region, the C^{6+} concentration decreases, and the local recycling C^{2+} mainly created by the free-streaming energetic D^{+} dominates the tungsten erosion. The width of the C^{6+} dominated region is determined by the C^{6+} concentration at the strike point and its decay length relative to that of the deuterium ion flux. The C^{6+} concentration at the strike point is assumed to be the same value as that at the separatrix at the OMP, which can be inferred from CER data. For all the three different discharges modeled, the intra-ELM C^{6+} concentrations at the OMP are at the level of 2%. The relative decay length of C^{6+} to D^{+} has a strong relationship with the energy carried by ELMs. The higher heat flux density discharge is expected to have a smaller relative decay length and thus a narrower C^{6+} dominated region. The FSM analysis of the ELM characters in this work shows that the high charge state impurities originated from in the pedestal region can play an important role in W erosion during an ELM burst. Thus, it is necessary to accurately evaluate the charge state of the energetic impurities during ELMs in a mixed-materials environment such as in ITER. These findings should have significant implications for future rectors, which will have mixed material environment, i.e., with mixed plasma-facing materials, and/or with impurity seeding for the control of heat flux and erosion control.

Note that the electron density dependence of W S/XB is still not well known, which may thus lead to some uncertainty in the analysis. In the intra-ELM semi-analytic model, the carbon redeposition fraction is assumed to be 0.7 according to the value of inter-ELM DIVIMP simulations. However, due to the high plasma density near the target during ELMs, the eroded carbon particles may be subject to strong friction and thus may have a greater chance to redeposit on the target. With an assumption that the redeposition fraction is changed from 0.7 to 0.9, the W erosion cause by redeposited carbon would increase by 40%. However, since the W erosion in the near separatrix region is dominated by the free-streaming C^{6+}, this will not change the main conclusions of this paper.

Note also that during ELMs, the peak impact

energy of streaming ions have a strong relationship with the electron temperature on the pedestal top [24,31]. The average intra-ELM impact energy of D^+ for the 'high frequency/small size' discharge is actually higher than the other two discharges because of the higher pedestal electron temperature. However, the D^+ impact energy is still too low to give a comparable W erosion to the C^{6+} during ELMs. Whereas for future fusion devices, which will have a much higher pedestal electron temperature, the direct W erosion by the streaming energetic D^+ may be dominant.

Furthermore, we should mention that the target recycling process is not included in the FSM in our analysis. As discussed in [15], if the particle recycling process is taken into consideration, the particle flux carried by ELM should be smaller than the Langmuir probe measurements, but the energy carried by deuterium should be larger, thus offsetting the effect of the flux reduction. Furthermore, in contrast to [15], this paper focuses on modeling the ELM-averaged target tungsten erosion profiles instead of the evolution of W erosion during ELMs. Since the ELM-averaged deuterium impact energy is smaller than the peak deuterium impact energy, the deuterium impact to the W erosion should be further reduced.

Acknowledgements

The authors would like to thank M. Knolker for the help of handling IR camera data. We are grateful to I. Bykov for helpful discussions. The work was performed under the auspices of the CSC (No.201506340019) and the U.S. Department of Energy, Office of Science, Office of Fusion Energy Sciences, using the DIII-D National Fusion Facility, a DOE Office of Science user facility, under Awards DE-FC02-04ER54698 and DE-SC0018423. The work was also supported by the National Natural Science Foundation of China (Grant No. 11535013) and the National Key Research and Development Program of China (Grant No. 2017YFE0301305). DIII-D data shown in this paper can be obtained in digital format by following the links at https://fusion.gat.com/global/D3D_DMP.

Disclaimer: DISCLAIMER: This report was prepared as an account of work sponsored by an agency of the United States Government. Neither the United States Government nor any agency thereof, nor any of their employees, makes any warranty, express or implied, or assumes any legal liability or responsibility for the accuracy, completeness, or usefulness of any information, apparatus, product, or process disclosed, or represents that its use would not infringe privately owned rights. Reference herein to any specific commercial product, process, or service by trade name, trademark, manufacturer, or otherwise does not necessarily constitute or imply its endorsement, recommendation, or favoring by the United States Government or any agency thereof. The views and opinions of authors expressed herein do not necessarily state or reflect those of the United States Government or any agency thereof.

References

[1] Hirai T, Escourbiac F, Carpentier-Chouchana S, Fedosov A, Ferrand L, Jokinen T, Komarov V, Kukushkin A, Merola M and Mitteau R 2013 ITER tungsten divertor design development and qualification program *Fusion Eng. Des.* **88** 1798–801

[2] Pütterich T, Neu R, Dux R, Whiteford A D, O'Mullane M G and Summers H P 2010 Calculation and experimental test of the cooling factor of tungsten *Nucl. Fusion* **50** 25012

[3] Neu R, Bobkov V, Dux R, Fuchs J C, Gruber O, Herrmann A, Kallenbach A, Maier H, Mayer M and Pütterich T 2009 Ten years of W programme in ASDEX Upgrade—Challenges and conclusions *Phys. Scr.* **2009** 14038

[4] Matthews G F, Beurskens M, Brezinsek S, Groth M, Joffrin E, Loving A, Kear M, Mayoral M L, Neu R and Prior P 2011 JET ITER-like wall—overview and experimental programme *Phys. Scr.* **2011** 14001

[5] Mayer M, Andrzejczuk M, Dux R, Fortuna-Zalesna E, Hakola A, Koivuranta S, Krieger K, Kurzydlowski K J, Likonen J and Matern G 2009 Tungsten erosion and redeposition in the all-tungsten divertor of ASDEX Upgrade *Phys. Scr.* **2009** 14039

[6] Mayer M, Krat S, Baron-Wiechec A, Brezinsek S, Coad P, Gasparyan Y, Heinola K, Jepu I, Likonen J and Petersson P 2018 Erosion and Deposition in the JET Divertor during the ITER-like Wall Campaigns *27th IAEA Fusion Energy Conference (FEC 2018)*

[7] Dux R, Bobkov V, Herrmann A, Janzer A, Kallenbach A, Neu R, Mayer M, Müller H W, Pugno R and Pütterich T 2009 Plasma-wall interaction and plasma behaviour in the non-boronised all tungsten ASDEX Upgrade *J. Nucl. Mater.* **390** 858–63

[8] Brezinsek S and contributors J-E 2015 Plasma-surface interaction in the Be/W environment: conclusions drawn from the JET-ILW for ITER *J. Nucl. Mater.* **463** 11–21

[9] Wong C P C, Junge R, Phelps R D, Politzer P, Puhn F, West W P, Bastasz R, Buchenauer D, Hsu W and Brooks J 1992 Divertor materials evaluation system at DIII-D *J. Nucl. Mater.* **196** 871–5

[10] Ding R, Stangeby P C, Rudakov D L, Elder J D, Tskhakaya D, Wampler W R, Kirschner A, McLean A G, Guo H Y and Chan V S 2015 Simulation of gross and net erosion of high-Z materials in the DIII-D divertor *Nucl. Fusion* **56** 16021

[11] Ding R, Rudakov D L, Stangeby P C, Wampler W R, Abrams T, Brezinsek S, Briesemeister A, Bykov I, Chan V S and Chrobak C P 2017 Advances in understanding of high-Z material erosion and re-deposition in low-Z wall environment in DIII-D *Nucl. Fusion* **57** 56016

[12] Abrams T, Ding R, Guo H Y, Thomas D M, Chrobak C P, Rudakov D L, McLean A G, Unterberg E A, Briesemeister A R and Stangeby P C 2017 The inter-ELM tungsten erosion profile in DIII-D H-mode discharges and benchmarking with ERO+ OEDGE modeling *Nucl. Fusion* **57** 56034

[13] Abrams T, Thomas D M, Unterberg E A and Briesemeister A R 2018 Advances in Low-Temperature Tungsten Spectroscopy Capability to Quantify DIII-D Divertor Erosion *IEEE Trans. Plasma Sci.*

[14] Xu G L, Guterl J, Abrams T, Wang H Q, Zhang P F, Elder J D, Unterberg E A, Thomas D M, Guo H Y and Ye M Y 2019 Study of DIII-D tungsten erosion processes by using a carbon–tungsten mixed material model *Nucl. Mater. Energy* **18** 141–6

[15] Abrams T, Unterberg E A, McLean A G, Rudakov D L, Wampler W R, Knolker M, Lasnier C,

Leonard A W, Stangeby P C and Thomas D M 2018 Experimental validation of a model for particle recycling and tungsten erosion during ELMs in the DIII-D divertor *Nucl. Mater. Energy* **17** 164–73

[16] Fundamenski W and Pitts R A 2005 A model of ELM filament energy evolution due to parallel losses *Plasma Phys. Control. fusion* **48** 109

[17] Stangeby P C, Elder J D, Boedo J A, Bray B, Brooks N H, Fenstermacher M E, Groth M, Isler R C, Lao L L and Lisgo S 2003 Interpretive modeling of simple-as-possible-plasma discharges on DIII-D using the OEDGE code *J. Nucl. Mater.* **313** 883–7

[18] Stangeby P C and Elder J D 1992 Calculation of observable quantities using a divertor impurity interpretive code, DIVIMP *J. Nucl. Mater.* **196** 258–63

[19] Hofsäss H, Zhang K and Mutzke A 2014 Simulation of ion beam sputtering with SDTrimSP, TRIDYN and SRIM *Appl. Surf. Sci.* **310** 134–41

[20] Watkins J G, Taussig D, Boivin R L, Mahdavi M A and Nygren R E 2008 High heat flux Langmuir probe array for the DIII-D divertor plates *Rev. Sci. Instrum.* **79** 10F125

[21] Hill D N, Ellis R, Ferguson W, Perkins D E, Petrie T and Baxi C 1988 Infrared thermography of the DIII-D divertor targets *Rev. Sci. Instrum.* **59** 1878–80

[22] Eldon D, Bray B D, Deterly T M, Liu C, Watkins M, Groebner R J, Leonard A W, Osborne T H, Snyder P B and Boivin R L 2012 Initial results of the high resolution edge Thomson scattering upgrade at DIII-D *Rev. Sci. Instrum.* **83** 10E343

[23] Chrystal C, Burrell K H, Grierson B A, Haskey S R, Groebner R J, Kaplan D H and Briesemeister A 2016 Improved edge charge exchange recombination spectroscopy in DIII-D *Rev. Sci. Instrum.* **87** 11E512

[24] Guillemaut C, Metzger C, Moulton D, Heinola K, O'Mullane M, Balboa I, Boom J, Matthews G F, Silburn S and Solano E R 2018 Experimental validation of an analytical kinetic model for edge-localized modes in JET-ITER-like wall *Nucl. Fusion* **58** 66006

[25] Manfredi G, Hirstoaga S and Devaux S 2010 Vlasov modelling of parallel transport in a tokamak scrape-off layer *Plasma Phys. Control. Fusion* **53** 15012

[26] Moulton D, Ghendrih P, Fundamenski W, Manfredi G and Tskhakaya D 2013 Quasineutral plasma expansion into infinite vacuum as a model for parallel ELM transport *Plasma Phys. Control. Fusion* **55** 85003

[27] Evans T E, Yu J H, Jakubowski M W, Schmitz O, Watkins J G and Moyer R A 2009 A conceptual model of the magnetic topology and nonlinear dynamics of ELMs *J. Nucl. Mater.* **390** 789–92

[28] Pamela S, Eich T, Frassinetti L, Sieglin B, Saarelma S, Huijsmans G, Hoelzl M, Becoulet M, Orain F and Devaux S 2015 Non-linear MHD simulations of ELMs in JET and quantitative comparisons to experiments *Plasma Phys. Control. Fusion* **58** 14026

[29] Huysmans G T A, Pamela S, Van Der Plas E and Ramet P 2009 Non-linear MHD simulations of edge localized modes (ELMs) *Plasma Phys. Control. Fusion* **51** 124012

[30] Guillemaut C, Jardin A, Horacek J, Borodkina I, Autricque A, Arnoux G, Boom J, Brezinsek S, Coenen J W and De La Luna E 2016 Experimental estimation of tungsten impurity sputtering due to Type I ELMs in JET-ITER-like wall using pedestal electron cyclotron emission and target Langmuir probe measurements *Phys. Scr.* **2016** 14005

[31] Guillemaut C, Jardin A, Horacek J, Autricque A, Arnoux G, Boom J, Brezinsek S, Coenen J W, De La Luna E and Devaux S 2015 Ion target impact energy during Type I edge localized

modes in JET ITER-like wall *Plasma Phys. Control. Fusion* **57** 85006

[32] Summers H P 1994 *Atomic data and analysis structure: user manual* (Joint European Torus)

[33] Den Harder N, Brezinsek S, Pütterich T, Fedorczak N, Matthews G F, Meigs A, Stamp M F, van de Sanden M C M, Van Rooij G J and Contributors J E T 2016 ELM-resolved divertor erosion in the JET ITER-like wall *Nucl. fusion* **56** 26014

[34] Eckstein W 2002 Calculated sputtering, reflection and range values

[35] Stangeby P C and Elder J D 1995 Impurity retention by divertors. I. One dimensional models *Nucl. fusion* **35** 1391

[36] Ueda Y, Fukumoto M, Sawamura I, Sakizono D, Shimada T and Nishikawa M 2006 Carbon impurity behavior on plasma facing surface of tungsten *Fusion Eng. Des.* **81** 233–9

[37] Shimada T, Funabiki T, Kawakami R, Ueda Y and Nishikawa M 2004 Carbon behavior on tungsten surface after carbon and hydrogen mixed beam irradiation *J. Nucl. Mater.* **329** 747–51

[38] Kawakami R, Shimada T, Ueda Y and Nishikawa M 2003 Dynamic behavior of tungsten surfaces due to simultaneous impact of hydrogen and carbon ion beam *Jpn. J. Appl. Phys.* **42** 7529

[39] Team A U, Eich T, Sieglin B, Scarabosio A, Fundamenski W, Goldston R J and Herrmann A 2011 Inter-ELM power decay length for JET and ASDEX Upgrade: measurement and comparison with heuristic drift-based model *Phys. Rev. Lett.* **107** 215001

[40] Stangeby P C 2012 The Chodura sheath for angles of a few degrees between the magnetic field and the surface of divertor targets and limiters *Nucl. Fusion* **52** 83012

[41] Xia T Y and Xu X Q 2015 Nonlinear fluid simulation of particle and heat fluxes during burst of ELMs on DIII-D with BOUT++ code *Nucl. Fusion* **55** 113030

[42] Chen B, Xu X Q, Xia T Y, Porkolab M, Edlund E, LaBombard B, Terry J, Hughes J W, Mao S F and Ye M Y 2017 Edge turbulence and divertor heat flux width simulations of Alcator C-Mod discharges using an electromagnetic two-fluid model *Nucl. Fusion* **57** 116025

[43] Xia T Y, Xu X Q and Xi P W 2013 Six-field two-fluid simulations of peeling–ballooning modes using BOUT++ *Nucl. Fusion* **53** 73009